RSC Advances

ROYAL SOCIETY OF CHEMISTRY

www.rsc.org/advances

Table of contents entry

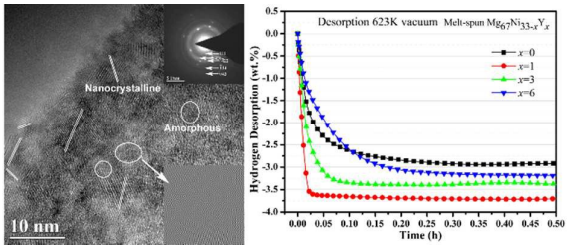

The high dehydrogenation kinetics are the results of low activation energy combined with amorphous and nanocrystalline structure.

Dehydrogenation behavior and microstructure evolution of hydrogenated Magnesium-Nickel-Yttrium melt-spun ribbons

Wenjie Song, Jinshan Li, Tiebang Zhang*, Xiaojiang Hou, Hongchao Kou

State Key Laboratory of Solidification Processing, Northwestern Polytechnical University, Xi'an 710072, PR China

*Corresponding author:

Tiebang Zhang

Address: 127 Youyi Xilu, Xi'an 710072, R.P. China

Tel: +86 29 88491764

Fax: +86 29 88460294

E-mail: tiebangzhang@nwpu.edu.cn (Tiebang Zhang)

Abstract

This paper reports porous $Mg_{67}Ni_{33-x}Y_x$ (x = 0, 1, 3, 6) ribbons which are prepared by a melt spinning method. The dehydrogenation behaviors, including the thermal decomposition process, dehydrogenation capacities, percent and kinetics, are investigated in a temperature range of 523-623 K. The microstructure evolution during dehydrogenation process of metal melt-spun ribbons is discussed in the aspect of the microstructures of hydrogenated and dehydrogenated ribbons. It is considered that the porous structure in the as-prepared ribbons accelerates the diffusion of hydrogen gas and atoms, and increases dehydrogenation nucleation locations and decreases the diffusion distance. Additionally, the addition of Y elements and melt-spinning decreases the activation energy of dehydrogenation. Low activation energy and refined microstructure play a dominant role in decreasing the dehydrogenation temperature and increasing the kinetics of Mg-based metal melt-spun ribbons.

Keywords: hydrogen storage; rapid solidification; nanocrystalline; rare earth; activation energy

1. Introduction

Magnesium-based alloys are considered as an promising medium of hydrogen storage for on-board vehicle and stationary applications on solving environment and energy issues, due to the high theoretical storage capacity (e.g. Mg 7.6 wt. %), light weight and abundant resources. However, the magnesium-based alloys have a high stability of the hydrides and low hydrogen atoms diffusion rate, which arouse the high dehydrogenation temperature and low hydrogen desorption kinetics, and limit it in industrial applications.[1]

A great many of efforts have been devoted to improving the dehydrogenation properties of the Mg-based alloys from two aspects, element doping and microstructure modification. The work has proved that the addition of transition metal elements,[2, 3] rare metal elements[4, 5] and catalysts[6, 7] into Mg-based alloys decreases the stability of hydrides and increases the dehydrogenation kinetics.[8] However, the excellent kinetics caused by the addition of transition metal elements are at the expense of low dehydrogenation capacities. It has been found that rare earth (RE) elements not only accelerate the dehydrogenation kinetics, but also enhance the dehydrogenation capacity comparing with transition metal elements by substituting B side elements of A_2B-type Mg-based alloy, and decrease the hydrogen desorption temperature.[9] By adding rare earth elements, the high activation of rare earth elements has catalysis on the decomposition of hydrogen molecules on the surface of alloy particles.[10] During the dehydrogenation process, the compounds and RE hydrides could be formed in the alloys and these products proven to provide positive catalysis on the formation and decomposition of other hydrides.[11] Especially, the yttrium (Y) is lighter than other RE elements, it is favorable to increase gaseous hydrogen absorption/desorption capacities per unit mass. Additionally, the strain and defects, which are induced by the formation and decomposition of YH_2/YH_3, are proved to facilitate the hydrogen absorption and desorption.[10] The addition of elements and catalysts can significantly improve the

hydrogenation/dehydrogenation rates,[12] however, these methods still cannot solve the problems of slow dehydrogenation kinetics well.[13]

The microstructure is closely related to the thermodynamic and kinetics of hydrogenation/dehydrogenation.[8] The diffusion of hydrogen atoms in alloys and hydrides is an important factor to the hydrogen desorption kinetics. The refined grain size to nanoscale and amorphous structure can significantly enhance the hydrogen absorption/desorption kinetics and hydrogen storage capacity since the refined grain generates a large amount of interfaces along which hydrogen atoms can diffuse more easily.[14, 15] For microstructure modification, ball milling[16] and melt spinning[17] are proved to be powerful techniques to produce amorphous and nanocrystalline Mg_2Ni alloys.[8] However, ball milling is still limited to some unavoidable shortcomings: contamination of metal powders by milling equipment and oxygen even in argon atmosphere,[18] small scale production and requires relatively high cost for special safe handling the powder such as heat-transfer and pipe blockage.[3] In addition, the growth of ball milled particle occurs at high reaction temperature and deteriorates the kinetic properties.[19] On the contrary, the microstructure stability of melt spun ribbons is higher than that of ball milled particles during the hydrogenation and dehydrogenation cycles.[8, 20] Generally speaking, the amorphous and nanocrystalline Mg-based alloys prepared by melt-spun have faster hydrogen absorption and desorption kinetics.[21] Melt spinning has been proven as an effective method to reduce the grain size and possesses attractive hydrogenation/dehydrogenation properties.[22] In addition to the enhanced diffusivity of hydrogen atoms, the diffusion distance is also decreased by melt spinning. The melt-spun ribbons can absorb and release hydrogen from two sides, therefore the ribbons can be hydrogenated completely with the thickness less than 50 μm.[23] In addition, increased porosity in metals significantly increases the diffusion of gas.[24] The dehydrogenation property is closely related to the microstructure, the microstructure evolution during dehydrogenation process is necessary to analyze the dehydrogenation mechanism of melt spun ribbons.

The two important factors on hydrogen desorption kinetics are dehydrogenation energy barrier of hydrides and the diffusion of hydrogen atoms. The addition of RE elements facilitates the glass forming of Mg_2Ni-based alloys.[8] The melt spinning technique combined with the addition of Y element into Mg_2Ni alloys is employed in this work to decrease the dehydrogenation energy barrier of hydrides and facilitate the diffusion of hydrogen atoms. Special attentions have been paid to the microstructure evolution and phase transformation of Y-doped Mg-based melt-spun ribbons during dehydrogenation process. The activation energy of the dehydrogenation reaction is calculated by the Kissinger method. In addition, the effect of temperature on dehydrogenation kinetics is also emphasized and the corresponding influencing factors are discussed. The corresponding dehydrogenation mechanism of Mg-Ni-Y melt-spun ribbons is proposed in this work.

2. Experimental

Mg-based hydrogen storage alloys with the composition of $Mg_{67}Ni_{33-x}Y_x$ (x = 0, 1, 3, 6 at. %) were melted under the protection of covering flux in a resistance furnace. The alloys were re-melted and spun on a single copper roller with linear velocity 40 ms^{-1} in an argon atmosphere of 500 mbar.[25] The melt-spun ribbons were about 50 μm in thickness, 5 mm in width and 10-30 mm in length. The ribbons which are prepared by melt-spinning technique were directly hydrogenated in an automatic Sieverts apparatus (PCT Pro2000) under initial hydrogen pressure of 30 bar at two temperatures of 523 and 623 K for 4 h. The dehydrogenation kinetics were measured under initial vacuum at corresponding hydrogenation temperature for 1 h. Before hydrogenation/dehydrogenation measurements, all the alloy ribbons were activated by three continuous hydrogenation/dehydrogenation cycles maintaining a initial hydrogen pressure of 30 bar at 10h for hydrogenation and vacuuming 1 h for dehydrogenation. The metallographic samples were prepared without any etching reagent even water. The phase composition and microstructure of the hydrogenated ribbons were characterized by X-Ray Diffraction (XRD), Scanning Electron Microscopy (SEM, TESCAN, MIR A3 XMU) and

Transition Electron Microscope (TEM, TECNAI, F30 G^2). The phase transformations during dehydrogenation of the hydrogenated ribbons were analyzed by Differential Scanning Calorimeter (DSC, NETZSCH, STA449C) at various heating rate of 5, 10, 15 and 20 K/min from ambient temperature to 723 K in an argon atmosphere.

3. Results and discussion

3.1 Phase analysis of hydrogenated ribbons

The XRD patterns of the hydrogenated $Mg_{67}Ni_{33-x}Y_x$ (x = 0, 1, 3, 6) melt-spun ribbons are shown in **Fig. 1**a. The dominant phase of the hydrogenated $Mg_{67}Ni_{33-x}Y_x$ (x = 0, 1, 3, 6) melt-spun ribbons is monoclinic Mg_2NiH_4. Bragg peaks of $Mg_2NiH_{0.3}$ and MgH_2 are also observed in the XRD patterns. In addition, several Bragg peaks of $MgYNi_4$, YH_2, YH_3 and cubic structure Mg_2NiH_4 phases are observed in XRD pattern of the hydrogenated ribbon with x = 6. The intensity (counts) of Bragg peaks of MgH_2 phase (~ 27.9°) increases from 599 to 2375 with the increasing Y content in the hydrogenated $Mg_{67}Ni_{33-x}Y_x$ (x = 0, 1, 3, 6) melt-spun ribbons. It indicates that the phase content of MgH_2 increases with the increase of Y content, which coincides with the content of reactant α-Mg phase in melt-spun ribbons.[25] On the contrary, the phase content of $Mg_2NiH_{0.3}$ decreases with the increase of Y content, which can be seen from the decreased intensities of Bragg peaks from $Mg_2NiH_{0.3}$ (about 21, 37 and 47°). $Mg_2NiH_{0.3}$ is a transitional phase of Mg_2Ni-Mg_2NiH_4 system. The addition of Y is beneficial to decrease the content of transitional phase $Mg_2NiH_{0.3}$ by facilitating the transformation of $Mg_2NiH_{0.3}$ to Mg_2NiH_4. The hydride of $MgYNi_4$ is not observed in the XRD patterns of the hydrogenated melt-spun ribbons because the $MgYNi_4$ absorbs hydrogen reversibly at room temperature,[26] and almost all of the hydrogen is released under 500 K.[27] The formation of hydride YH_2, as the catalyst, facilitates the forming of $Mg_2NiH_{0.3}$ and MgH_2 during hydrogenation process.[11] Then the $Mg_2NiH_{0.3}$ and YH_2 are completely hydrogenated to Mg_2NiH_4 and YH_3, respectively. The strain and defects induced by YH_2/YH_3 are believed to facilitate the hydrogenation/dehydrogenation process.[11]

Fig. 1b shows the XRD patterns of the dehydrogenated $Mg_{67}Ni_{33-x}Y_x$ (x = 0, 1, 3, 6) ribbons. The dominant phase of dehydrogenated $Mg_{67}Ni_{33-x}Y_x$ ribbons is Mg_2Ni. The $MgNi_2$, which is eliminated by the melt-spun technique, is separated out from the dehydrogenated ribbons after 4 hydrogenation/dehydrogenation cycles. The Bragg peak intensity of $MgNi_2$ decreases with the increase of Y in the dehydrogenated ribbons. The Bragg peaks of Mg (~ 43.3°) and $MgYNi_4$ (~ 42.7°) are in the dehydrogenated $Mg_{67}Ni_{33-x}Y_x$ (x = 1, 3, 6) ribbons, their intensities increase with the increasing Y in the dehydrogenated ribbons. The YH_2, which is an incomplete dehydrogenated product of YH_3, also appears in the Bragg peaks of dehydrogenated $Mg_{67}Ni_{33-x}Y_x$ ribbons with x = 6. The phases of dehydrogenated ribbons are similar with those of the melt-spun ribbons[25] except for the addition of $MgNi_2$ and YH_2 after 4 hydrogenation/dehydrogenation cycles.

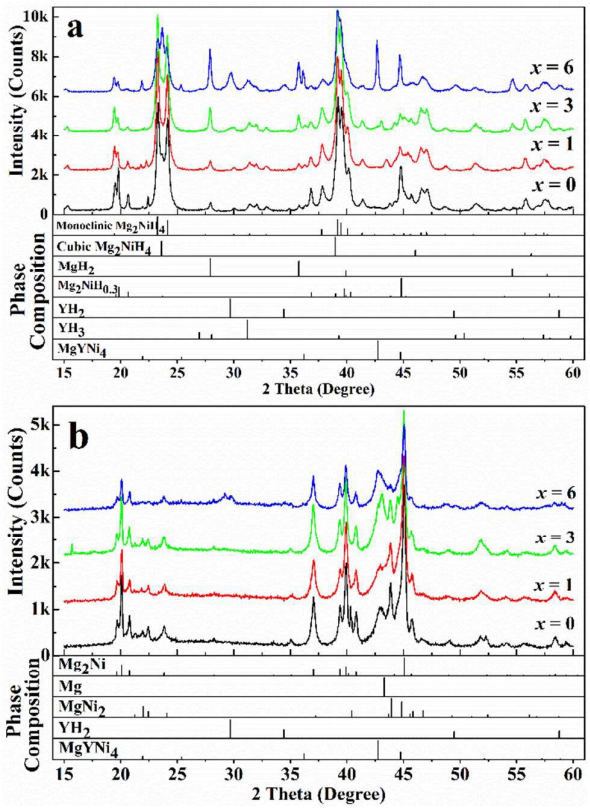

Fig. 1. The XRD patterns of the (a) hydrogenated and (b) dehydrogenated $Mg_{67}Ni_{33-x}Y_x$ (x = 0, 1, 3, 6) melt-spun ribbons.

From comparing the phase structures of the hydrogenated and dehydrogenated samples, the phase transformations contain Mg_2NiH_4 to Mg_2Ni, $Mg_2NiH_{0.3}$ to Mg_2Ni, MgH_2 to Mg and YH_3 to YH_2. The $MgYNi_4$ phase appears both in hydrogenated and dehydrogenated samples, but the hydride of $MgYNi_4$ is not observed. The hydride of $MgYNi_4$ is dehydrogenated in the experimental condition probably.[27] In addition, trace $MgNi_2$ phase precipitates out in 4 hydrogenation/dehydrogenation cycles. The broadening of XRD patterns indicates that amorphous/nanocrystalline are included in the hydrogenated and dehydrogenated ribbons.

3.2 Microstructures of hydrogenated ribbons

The crystallite sizes of ribbons increase from 5 nm to 150 nm with addition of Y content in the melt-spun $Mg_{67}Ni_{33-x}Y_x$ (x = 1, 3, 6) ribbons. **Fig. 2** shows the high resolution image of hydrogenated ribbons, the corresponding Selected Area Electron Diffraction (SAED) pattern and Electron Energy-Loss Spectroscopy (EELS) hydrogen mapping. The ribbons contain amorphous and nanocrystalline as shown in **Fig. 2**a, which is consistent with the results of XRD. The circled area is amorphous and the straight-line portion is nanocrystalline. In addition, the continuous rings with scattered diffraction points of SAED pattern also indicate that the microstructures of ribbons are amorphous and nanocrystalline. Nanocrystalline hydrides enhance the hydrogenation kinetics.[28] The SAED pattern shows that the ribbons are polycrystalline in a electron beam diameter. The major phase Mg_2NiH_4 is observed in the hydrogenated ribbons in the polycrystalline SAED rings. It has been proven that the amorphous and nanocrystalline can provide passageways for the diffusion of hydrogen atoms.[29] The grains of the hydrogenated ribbons are refined for the effect of melt-spun. The amorphous and nanocrystalline by melt-spun can shorten the diffusion distance and enhance the diffusivity of hydrogen.

The High Resolution Transmission Electron Microscopy (HRTEM) image and the corresponding Fast Fourier Transform (FFT) pattern of the hydrogenated $Mg_{67}Ni_{33-x}Y_x$ (x = 3) ribbon are shown in **Fig. 2**b. The amorphous structure and nanocrystalline are observed in the

HRTEM image. The FFT pattern is an amorphous ring with slight scattered diffraction points. **Fig. 2**c shows the HRTEM image of the hydrogenated $Mg_{67}Ni_{33-x}Y_x$ (x = 6) ribbons. The interplanar spacing and Miller indices of Mg_2NiH_4 are marked in the HRTEM image and SAED pattern. A lot of stacking faults are observed in the HRTEM image. Crystal defects are induced by hydrogen absorption/desorption in Mg_2Ni and other hydrogen storage alloys.[30] It has been reported that the stacking faults are beneficial to the nucleation of hydrides and lead to lower hydrogen desorption temperature and better kinetics.[31] Comparing with the ribbons with x = 1 and 3, the hydrogenated ribbons with x = 6 contain more crystalline structures as shown in Fig 2c. Plenty of amorphous structures are observed in the melt-spun ribbons of x =6 before hydrogenation. The crystallization of amorphous structure is occurred in hydrogenation process.[21] In addition, stacking faults are formed in the crystallization process. It has been reported that changing the structure of the Mg_2Ni alloy from polycrystalline to nanocrystalline results in a drop of about 100 K in absorbing/desorbing temperature.[32] The amorphous alloy exhibits faster hydrogenation kinetics than the crystallized alloy with the same composition due to the faster hydrogen diffusion in the amorphous phase.[4] Amorphous and nanocrystalline is helpful to the hydrogenation/dehydrogenation.

In order to analyze the distribution of hydrides, the EELS hydrogen mapping is characterized as shown in **Fig. 2**d. The white portion is the area including hydrogen atoms. The dark particle surface gives the evidence that partial hydrogen atoms release from the particle surface under the high vacuum of the TEM and the effect of electron beam. The hydrogen desorption process has been clearly seen in the EELS maps at ~400°C,[33] but the Mg-based hydrides are rather stable at room temperature. The SAED pattern shows that the ribbons have been hydrogenated and the dominant hydride can be ascribed to Mg_2NiH_4.

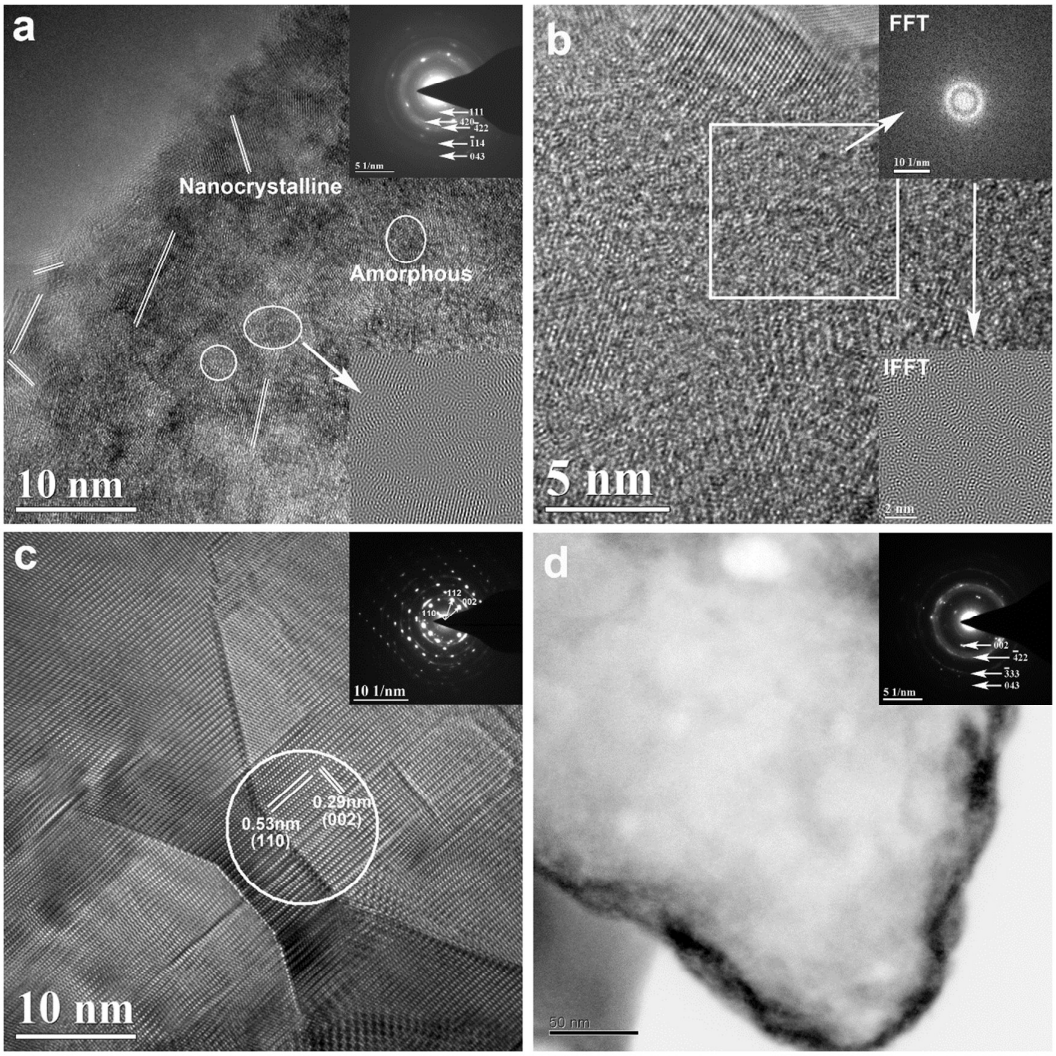

Fig. 2. HRTEM image and SAED pattern of the $Mg_{67}Ni_{33-x}Y_x$ (x = 1, 3, 6) ribbons and EELS hydrogen mapping. a) x = 1, b) x = 3, c) x = 6, d) EELS hydrogen mapping of x = 3 ribbons.

3.3 Microstructure evolution during dehydrogenation

The dehydrogenation process of ball milled particles has been described by Tanniru *et al.*[34] However, the dehydrogenation process of melt-spun ribbon has not been described. In order to analyze the dehydrogenation process, the microstructures of hydrogenated and dehydrogenated melt-spun ribbons are analyzed in this work as shown in **Fig. 3**. Plenty connected pores, which have been observed in the microstructure of melt-spun ribbons,[25] are also observed in the microstructure of hydrogenated and dehydrogenated ribbons after 4

hydrogenation/dehydrogenation cycles. Owing to the insulativity and lower z-contrast (atomic number) of the hydride, the hydride phase appears darker than the metal phase in the BSE mode.[35, 36] The areas around the pores are preferentially hydrogenated as shown in **Fig. 3**a. The process of hydrogen desorption is an inverse process of the absorption.[37] The areas around the pores in melt spun ribbons are similar to the surface of ball milled particles. The areas around the pores are the preferential position of dehydrogenation. The cracks can be observed in the dehydrogenated ribbons as shown in **Fig. 3**b. The hydrogen absorption and desorption of alloys result in the expansion and contraction of crystal lattice during the hydrogenation/dehydrogenation cycles, inducing stress in the grain. The hydrogenation/dehydrogenation cycles increase the brittleness of the ribbons, but seriously pulverization have not happened. The melt spun ribbons are distorted during hydrogenation/dehydrogenation cycles and the distortion counteracts partial distortion energy. Plenty amorphous and nanocrystalline in the melt-spun ribbons provide more diffusion paths for hydrogen atoms. The grain size reduced to nanoscale decreases the diffusion distance. The porous surface structure increases the hydrogen absorption rate.[28] Hydrogen diffusion through the bulk metal (hydride) phase is usually quite slow and often rate-limiting.[38] Hydrogen diffusion in gaseous phase is fast greater than that in bulk metal phase. It has been reported that fast hydrogen diffusion through or along the porous carbon phase benefit the kinetics of hydrogen release and uptake.[38] The pores in the melt-spun ribbons provide plenty of surfaces, increasing dehydrogenation nucleation location and decreasing the diffusion distances. In addition, the released hydrogen gas can be exhausted from the ribbons by the connected pores, further improving the hydrogen desorption kinetics. The areas around the pores are the preferential position for hydrogenation/dehydrogenation.

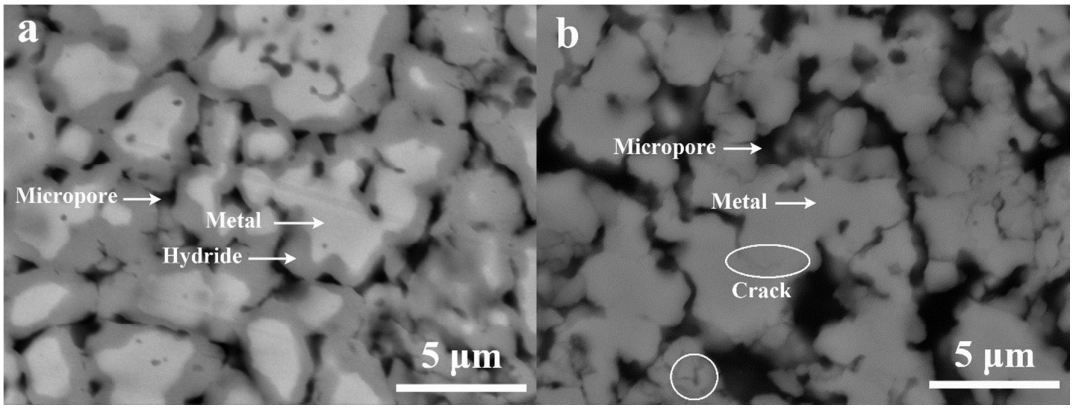

Fig. 3. The SEM/BSE images of (a) hydrogenated and (b) dehydrogenated melt-spun ribbons.

3.4 Thermal decomposition behavior of hydrogenated ribbons

Fig. 4a shows the dehydrogenation DSC curves and the corresponding first derivative curves (DDSC) of hydrogenated $Mg_{67}Ni_{33-x}Y_x$ (x = 0, 1, 3, 6) melt-spun ribbons at heating rate of 10 K/min. The obvious endothermic peak around 520~560 K observed in each DSC curve can be ascribed to the dehydrogenation peak of the dominant Mg_2NiH_4 phase. The dehydrogenation phases are Mg_2NiH_4, $Mg_2NiH_{0.3}$, MgH_2 and YH_3 from the phase analysis. The dehydrogenation peak of the intermediate hydride $Mg_2NiH_{0.3}$ phase overlaps Mg_2NiH_4. The dehydrogenation temperature of MgH_2 is higher than that of Mg_2NiH_4, the endothermic peak of MgH_2 powder is about 664 K, but it is still over 593 K in the $Mg_{80}Ni_{10}Y_{10}$ alloy with the addition of Ni and Y.[9] The trace endothermic peaks of MgH_2 in **Fig. 4a** are about 600 ~ 660 K for the minor content of MgH_2. It has been reported that the desorption temperature of YH_3 into YH_2 in vacuum starts at 443 K and the peak temperature is 533 K.[39] The endothermic peak of YH_3 to YH_2 overlaps that of Mg_2NiH_4 in the $Mg_{67}Ni_{33-x}Y_x$ ribbon with x = 6. The main endothermic peak of Mg_2NiH_4 is not symmetric, peaks overlap on the main endothermic peak as can be seen in the DDSC curve. The decomposition of Mg_2NiH_4 is divided into two steps, which are dehydrogenation of Mg_2NiH_4 to $Mg_2NiH_{0.3}$ and dehydrogenation of $Mg_2NiH_{0.3}$ to Mg_2Ni.[40] Therefore, the main dehydrogenation peaks contain overlapping peaks. The area under the peaks reveals the heat of the absorption of ribbons per unit mass. The heat of the absorption of ribbon with x = 0 exceeds 1700 J/g, and it

is below 1300 J/g with x = 1, 3 and 6. The addition of Y decreases the heat of the absorption of ribbons per unit mass in dehydrogenation process.

It is obvious that the peak dehydrogenation temperature (~525K) of the melt-spun ribbon with x = 1 is lower compared with that of the melt-spun ribbons with x = 0, 3 and 6 (~542, ~539 and ~554 K, respectively) in **Fig. 4a**. In order to analyze the activation energy of the dehydrogenation reaction of Mg_2NiH_4, the dehydrogenation DSC curves of the hydrogenated $Mg_{67}Ni_{33-x}Y_x$ (x = 0, 1, 3, 6) melt-spun ribbons at heating rates of 5, 10, 15 and 20 K/min are measured and the DSC curves of x = 1 ribbons are shown in **Fig. 4b**. The corresponding dominated dehydrogenation peak temperatures of $Mg_{67}Ni_{33-x}Y_x$ (x = 0, 1, 3, 6) melt-spun ribbons are summarized in **Table 1**. The Arrhenius equation,[41] $k = A\exp(-\frac{E_a}{RT})$, indicates that the lower activation energy E_a is related to faster reaction rate k and lower temperature T. The apparent activation energy for dehydrogenation of dominate phase Mg_2NiH_4 in the hydrogenated $Mg_{67}Ni_{33-x}Y_x$ (x = 0, 1, 3, 6) ribbons is calculated based on the dehydrogenation peak temperatures in **Table 1** using the Kissinger equation (**Equation 1**).[42]

$$\ln(\frac{\beta}{T_p^2}) = \ln(\frac{A_k R}{E_k}) - \frac{E_k}{RT_p} \quad (1)$$

Where β is the heating rate, T_p is the peak temperature, A_k is the preexponential factor, E_k is the dehydrogenation activation energy, R is the gas constant (8.3145 J (K mol)$^{-1}$). $\ln(\beta/T_p^2)$ and $1/T_p$ are linear correlation. Fitting curves of the hydrogenated $Mg_{67}Ni_{33-x}Y_x$ (x = 0, 1, 3, 6) melt-spun ribbons by the Kissinger method present a good linear relation between $\ln(\beta/T_p^2)$ and $1/T_p$ with a slop of $-E_k/R$, as shown in **Fig. 5a**. The activation energy E_k of the $Mg_{67}Ni_{33-x}Y_x$ (x = 0, 1, 3, 6) ribbons in the dehydrogenation can be summarized as 102, 73, 98 and 80 kJ/mol by Kissinger equation,[42] respectively. The E_k of melt-spun ribbons with x = 0 is 102 kJ/mol, which is closed to the Mg_2NiH_4.[43] The trend line of activation energy of the $Mg_{67}Ni_{33-x}Y_x$ (x = 0, 1, 3, 6) ribbons is shown in **Fig. 5b**. The dehydrogenation activation energy of the ribbons with x = 1, 3, 6 is lower than that of the hydrogenated ribbon with x = 0 with the

addition of Y. The hydrogenated melt-spun ribbon with $x = 1$ possesses the lowest activation energy of the dehydrogenation reaction among experimental alloys. The small quantity addition of Y element and refinement of the particles and grains decrease the apparent activation energy for hydrogen desorption by shortening the diffusion distance and enhancing the diffusivity with the increase of the micro strain and lattice distortion.[44] YH_2 and YH_3 are generated in the Mg-based alloys in hydrogenation and dehydrogenation processes. Fine YH_2/YH_3 particles provide large amount of active sites and paths to enhance the H atom diffusion along abundant phase boundaries and hydride phases.[45] The refined grain size of alloys, multiphase structure and YH_2/YH_3 decrease the activation energy during dehydrogenation.

Table 1. The dehydrogenation peak temperatures of the hydrogenated $Mg_{67}Ni_{33-x}Y_x$ (x = 0, 1, 3, 6) melt-spun ribbons at heating rates of 5, 10, 15 and 20 K/min.

Composition	Dehydrogenation peak temperature			
$Mg_{67}Ni_{33-x}Y_x$	5 K/min	10 K/min	15 K/min	20 K/min
$x = 0$	527	542	553	556
$x = 1$	507	525	534	547
$x = 3$	526	539	549	557
$x = 6$	538	554	568	577

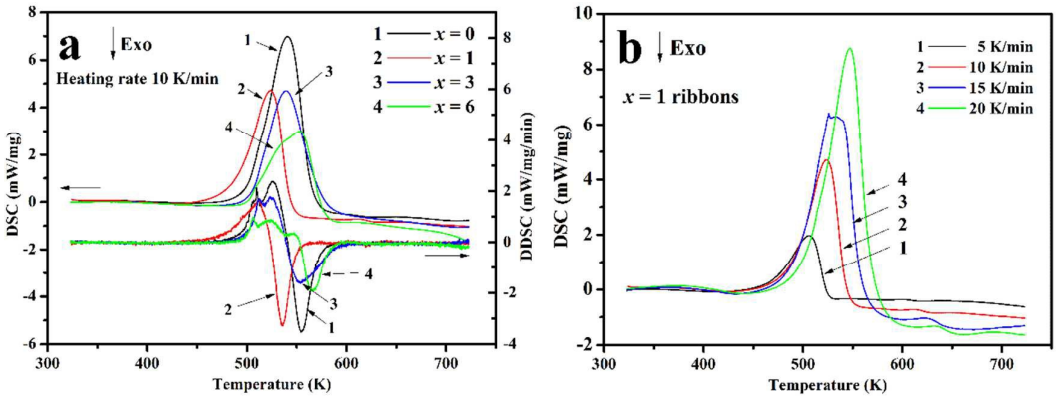

Fig. 4. Dehydrogenation DSC and corresponding first derivative curves of the hydrogenated $Mg_{67}Ni_{33-x}Y_x$ (x = 0, 1, 3, 6) melt-spun ribbons. a) heating rate of 10 K/min in $Mg_{67}Ni_{33-x}Y_x$ (x = 0, 1, 3, 6) melt-spun ribbons, b) heating rates of 5, 10, 15 and 20 K/min in x = 1 ribbons.

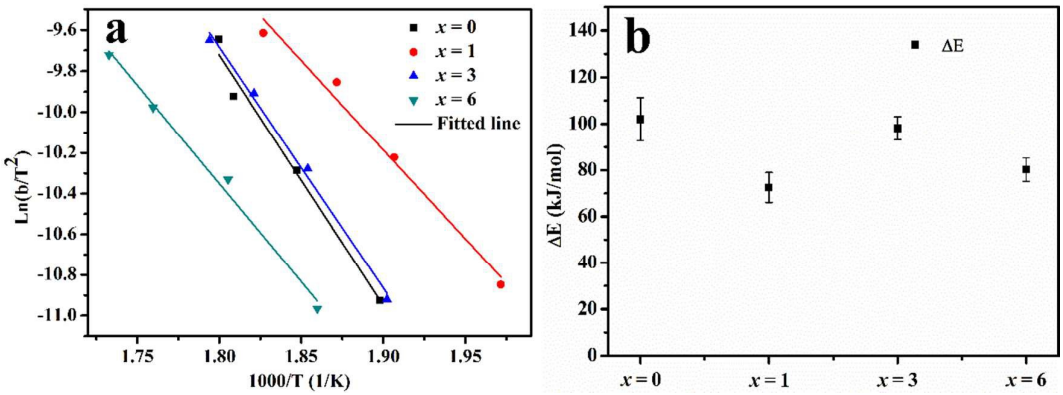

Fig. 5. Fitted Kissinger curves and corresponding dehydrogenation activation energy curves of the hydrogenated $Mg_{67}Ni_{33-x}Y_x$ (x = 0, 1, 3, 6) ribbons. a) fitted Kissinger curves, b) the activation energy curves of dehydrogenation reaction

3.5 Dehydrogenation kinetics

The activation energy is related to the reaction temperature as well as the reaction kinetics. The hydrogen desorption capacities of the $Mg_{67}Ni_{33-x}Y_x$ (x = 0, 1, 3, 6) ribbons detected at 523 and 623 K are shown in **Fig. 6**. The hydrogen desorption capacities of all the ribbons added with Y are higher than $Mg_{67}Ni_{33-x}Y_x$ (x = 0) ribbons at 523, 573 [25] and 623K. The addition of Y decreases the activation energy of the dehydrogenation reaction and increases the hydrogen desorption capacity corresponding with $Mg_{67}Ni_{33-x}Y_x$ (x = 0) ribbons. The $Mg_{67}Ni_{33-x}Y_x$ ribbons are not dehydrogenated completely at the same hydrogenation temperature from the dehydrogenation percent in Fig. 6. It can be explained that partial hydrides (such as YH_2) do not release hydrogen at the temperature. In addition, the hydrogen desorption is related to the hydrogen pressure as well as the temperature.[46] The hydrogen pressure increases with the hydrogen desorption during the dehydrogenation process, and the partial hydrogen dissolved in the alloys is not released under the increased hydrogen pressure. Further decreasing the hydrogen pressure and raising temperature can facilitate the dehydrogenation of hydrides. The

contents of $MgYNi_4$ increase with the increasing Y content in the ribbons with x = 1, 3 and 6.[25] Mg is consumed by forming $MgYNi_4$ but the hydride of $MgYNi_4$ is not observed in the hyhrogenated ribbons. In addition, partial hydrides (such as YH_2) do not release hydrogen at the experimental temperature. The maximum dehydrogenation capacity of ribbons with x = 6 is lower than that of x = 3. The low activation energy of the dehydrogenation reaction makes it easy to release hydrogen. The ribbon with x = 1 has the maximum of dehydrogenation capacity in the $Mg_{67}Ni_{33-x}Y_x$ ribbons for the lowest activation energy of the dehydrogenation reaction. But the ribbon with x =1 has relatively high dehydrogenation percent even at 523K. The low activation energy of the dehydrogenation reaction of the $Mg_{67}Ni_{33-x}Y_x$ (x = 1) ribbon not only increases the hydrogen desorption capacity and kinetics but decreases the dehydrogenation temperature.

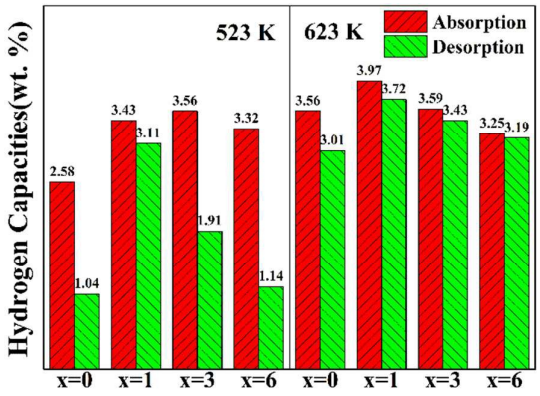

Fig. 6. Hydrogen desorption content of the $Mg_{67}Ni_{33-x}Y_x$ ribbons.

Fig. 7 shows the dehydrogenation kinetics curves of the $Mg_{67}Ni_{33-x}Y_x$ (x = 0, 1, 3, 6) ribbons at 523 and 623 K in initial 1 and 0.5 h. As can be seen from the kinetics curves, the dehydrogenation rates of ribbons at 523 K are lower than those at 623 K. The increase of temperature improves the dehydrogenation kinetics of ribbons. After the addition of Y, the dehydrogenation kinetics of the $Mg_{67}Ni_{33-x}Y_x$ (x = 1, 3, 6) ribbons are better than that of ribbons with x = 0 at 523 K. Considering the values of the activation energy of dehydrogenation, the values of $Mg_{67}Ni_{33-x}Y_x$ (x = 1, 3, 6) ribbons is lower than that of the ribbon with x = 0. The property of dehydrogenation kinetics is related to the activation energy

of dehydrogenation. In addition, the dehydrogenation kinetics is also related to the microstructure of the ribbons. The grain size of ribbons increases with the addition of Y elements. The dehydrogenation kinetics are the results of the activation energy of the dehydrogenation reaction combined with microstructure. The ribbon with $x = 1$ has the highest kinetics in the $Mg_{67}Ni_{33-x}Y_x$ ($x = 1, 3, 6$) ribbons at 523 and 623 K. The high dehydrogenation kinetics of $Mg_{67}Ni_{33-x}Y_x$ ribbons with $x = 1$ are also related to the high pore percentage.[25]

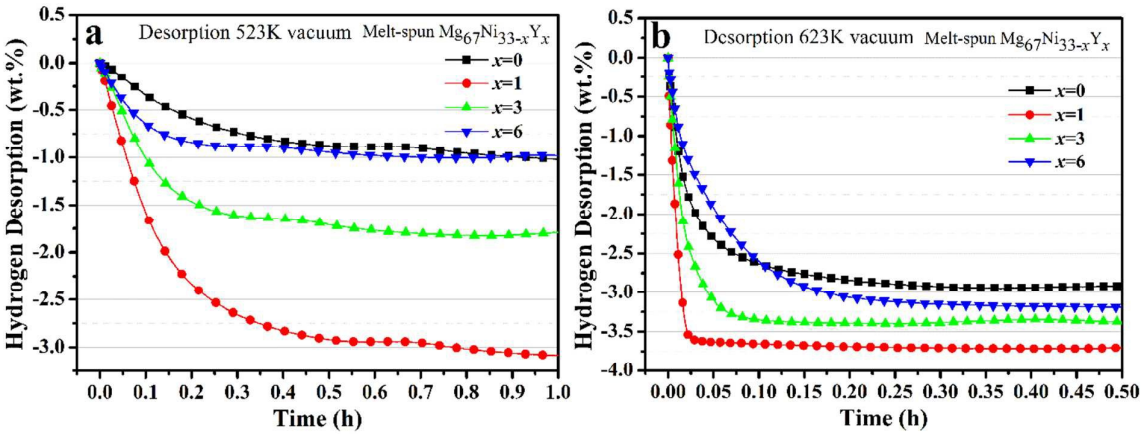

Fig. 7. The dehydrogenation kinetics curves of the $Mg_{67}Ni_{33-x}Y_x$ ($x = 0, 1$) ribbons at 523 and 623 K in initial 1 and 0.5 h. a) 523 K in initial 1h, b) 623 K in initial 0.5 h.

4. Conclusions

The dehydrogenation phase transformation contain Mg_2NiH_4 to Mg_2Ni, $Mg_2NiH_{0.3}$ to Mg_2Ni, MgH_2 to Mg and YH_3 to YH_2 of hydrogenated $Mg_{67}Ni_{33-x}Y_x$ ($x = 0, 1, 3, 6$) ribbons. Amorphous and nanocrystalline structures and stacking faults are contained in the $Mg_{67}Ni_{33-x}Y_x$ ($x = 0, 1, 3, 6$) ribbons. The H element is evenly distributed in the hydrogenated ribbons by EELS analysis. The pores in the melt-spun ribbons are the preferential areas for hydrogenation/dehydrogenation. The pores in metal ribbons generated by melt-spinning facilitate the diffusion of hydrogen, increase dehydrogenation nucleation locations and decrease the diffusion distances. The high dehydrogenation kinetics are the results of low activation energy combined with amorphous and nanocrystalline. The low activation energy

of the dehydrogenation reaction, caused by melt-spun and addition of Y elements, decreases the dehydrogenation temperatures and increases the dehydrogenation kinetics of Mg-based melt-spun ribbons.

Acknowledgements

This work is financially supported by the Doctorate Foundation of Northwestern Polytechnical University (CX201107) and Project supported by the Research Fund of the State Key Laboratory of Solidification Processing (NWPU) (95-QZ-2014). The Program of Introducing Talents of Discipline to Universities (B08040) is also acknowledged. Prof. Zhong-min Wang from Guilin University of Electronic Technology is gratefully appreciated for his help in hydrogen absorption/desorption measurements.

References

1. P. Vajeeston, P. Ravindran, B. C. Hauback, H. Fjellvåg, A. Kjekshus, S. Furuseth and M. Hanfland, *Phys Rev B*, 2006, **73**, 224102.
2. D. Vyas, P. Jain, J. Khan, V. Kulshrestha, A. Jain and I. P. Jain, *Int J Hydrogen Energy*, 2012, **37**, 3755-3760.
3. Y. H. Cho, S. Aminorroaya, H. K. Liu and A. K. Dahle, *Int J Hydrogen Energy*, 2011, **36**, 4984-4992.
4. Á. Révész, Á. Kis-Tóth, L. K. Varga, E. Schafler, I. Bakonyi and T. Spassov, *Int J Hydrogen Energy*, 2012, **37**, 5769-5776.
5. J. X. Zou, X. Q. Zeng, Y. J. Ying, X. Chen, H. Guo, S. Zhou and W. J. Ding, *Int J Hydrogen Energy*, 2013, **38**, 2337-2346.
6. R. K. Singh, H. Raghubanshi, S. K. Pandey and O. N. Srivastava, *Int J Hydrogen Energy*, 2010, **35**, 4131-4137.
7. X. J. Hou, R. Hu, T. B. Zhang, H. C. Kou, J. S. Li and X. Y. Xue, *Int J Hydrogen Energy*, 2013, **38**, 12904-12911.

8. Y. Zhang, T. Zhai, B. Li, H. Ren, W. Bu and D. Zhao, *J Mater Sci Technol*, 2014, **30**, 1020-1026.
9. S. Kalinichenka, L. Röntzsch, C. Baehtz and B. Kieback, *J Alloy Compd*, 2010, **496**, 608-613.
10. Z. N. Li, X. P. Liu, L. J. Jiang and S. M. Wang, *Int J Hydrogen Energy*, 2007, **32**, 1869-1874.
11. J. W. Liu, C. C. Zou, H. Wang, L. Z. Ouyang and M. Zhu, *Int J Hydrogen Energy*, 2013, **38**, 10438-10445.
12. S. Kalinichenka, L. Röntzsch and B. Kieback, *Int J Hydrogen Energy*, 2009, **34**, 7749-7755.
13. S. T. Sabitu, G. Gallo and A. J. Goudy, *J Alloy Compd*, 2010, **499**, 35-38.
14. X. J. Hou, R. Hu, T. B. Zhang, H. C. Kou and J. S. Li, *Int J Hydrogen Energy*, 2013, **38**, 16168-16176.
15. J. Cermák and L. Král, *Acta Mater*, 2008, **56**, 2677-2686.
16. Á. Révész and D. Fátay, *J Power Sources*, 2010, **195**, 6997-7002.
17. C. Pohlmann, B. Kieback and L. Röntzsch, *Int J Hydrogen Energy*, 2014, **39**, 8331-8339.
18. C. Suryanarayana, *Prog Mater Sci*, 2001, **46**, 1-184.
19. Y. S. Au, M. K. Obbink, S. Srinivasan, P. C. M. M. Magusin, K. P. de Jong and P. E. de Jongh, *Adv Funct Mater*, 2014, **24**, 3604-3611.
20. G. Y. Liang, D. C. Wu, L. Li and L. J. Huang, *J Power Sources*, 2009, **186**, 528-531.
21. Q. A. Zhang, L. X. Zhang and Q. Q. Wang, *J Alloy Compd*, 2013, **551**, 376-381.
22. E. A. Lass, *Int J Hydrogen Energy*, 2012, **37**, 9716-9721.
23. I. P. Jain, C. Lal and A. Jain, *Int J Hydrogen Energy*, 2010, **35**, 5133-5144.
24. V. Bérubé, G. Radtke, M. Dresselhaus and G. Chen, *Int J Energ Res*, 2007, **31**, 637-663.
25. W. J. Song, J. S. Li, T. B. Zhang, H. C. Kou and X. Y. Xue, *J Power Sources*, 2014, **245**, 808-815.

26. K. Aono, S. Orimo and H. Fujii, *J Alloy Compd*, 2000, **309**, L1-L4.
27. N. Hanada, S.-i. Orimo and H. Fujii, *J Alloy Compd*, 2003, **356–357**, 429-432.
28. B. Sakintuna, F. Lamari-Darkrim and M. Hirscher, *Int J Hydrogen Energy*, 2007, **32**, 1121-1140.
29. Y. H. Zhang, D. L. Zhao, S. H. Guo, Y. Qi, Z. W. Wu and X. L. Wang, *J Alloy Compd*, 2009, **476**, 457-461.
30. D. Liu, Y. Zhu and L. Li, *Int J Hydrogen Energy*, 2007, **32**, 2417-2421.
31. N. Takeichi, K. Tanaka, H. Tanaka, T. T. Ueda, Y. Kamiya, M. Tsukahara, H. Miyamura and S. Kikuchi, *J Alloy Compd*, 2007, **446–447**, 543-548.
32. L. H. Kumar, B. Viswanathan and S. S. Murthy, *J Alloy Compd*, 2008, **461**, 72-76.
33. K. Tanaka, T. Miwa, K. Sasaki and K. Kuroda, *J Alloy Compd*, 2009, **478**, 308-316.
34. M. Tanniru, H. Y. Tien and F. Ebrahimi, *Scripta Mater*, 2010, **63**, 58-60.
35. M. Vittori Antisari, A. Aurora, D. Mirabile Gattia and A. Montone, *Scripta Mater*, 2009, **61**, 1064-1067.
36. H.-Y. Tien, M. Tanniru, C.-Y. Wu and F. Ebrahimi, *Int J Hydrogen Energy*, 2009, **34**, 6343-6349.
37. K. C. Chou and K. Xu, *Intermetallics*, 2007, **15**, 767-777.
38. P. Adelhelm and P. E. de Jongh, *J Mater Chem*, 2011, **21**, 2417-2427.
39. V. A. Yartys, O. Gutfleisch, V. V. Panasyuk and I. R. Harris, *J Alloy Compd*, 1997, **253–254**, 128-133.
40. S. Kalinichenka, L. Röntzsch, C. Baehtz, T. Weißgärber and B. Kieback, *J Alloy Compd*, 2011, **509, Supplement 2**, S629-S632.
41. S. Arrhenius, *Zeitschrift für physikalische Chemie*, 1889, **4**, 226.
42. H. E. Kissinger, *Anal Chem*, 1957, **29**, 1702-1706.
43. I. C. Atias-Adrian, F. A. Deorsola, G. A. Ortigoza-Villalba, B. DeBenedetti and M. Baricco, *Int J Hydrogen Energy*, 2011, **36**, 7897-7901.

44. Y. P. Pang, Y. F. Liu, X. Zhang, M. X. Gao and H. G. Pan, *Int J Hydrogen Energy*, 2013, **38**, 1460-1468.

45. F. P. Luo, H. Wang, L. Z. Ouyang, M. Q. Zeng, J. W. Liu and M. Zhu, *Int J Hydrogen Energy*, 2013, **38**, 10912-10918.

46. L. Schlapbach and A. Züttel, *Nature*, 2001, **414**, 353-358.

Captions of figures and tables

Fig. 1. The XRD patterns of the (a) hydrogenated and (b) dehydrogenated $Mg_{67}Ni_{33-x}Y_x$ (x = 0, 1, 3, 6) melt-spun ribbons.

Fig. 2. HRTEM image and SAED pattern of the $Mg_{67}Ni_{33-x}Y_x$ (x = 1, 3, 6) ribbons and EELS hydrogen mapping. a) x = 1, b) x = 3, c) x = 6, d) EELS hydrogen mapping.

Fig. 3. The SEM/BSE images of (a) hydrogenated and (b) dehydrogenated melt-spun ribbons.

Fig. 4. Dehydrogenation DSC and corresponding first derivative curves of the hydrogenated $Mg_{67}Ni_{33-x}Y_x$ (x = 0, 1, 3, 6) melt-spun ribbons. a) heating rate of 10 K/min in $Mg_{67}Ni_{33-x}Y_x$ (x = 0, 1, 3, 6) melt-spun ribbons, b) heating rates of 5, 10, 15 and 20 K/min in x = 1 ribbons.

Fig. 5. Fitted Kissinger curves and corresponding activation energy curves of the hydrogenated $Mg_{67}Ni_{33-x}Y_x$ (x = 0, 1, 3, 6) ribbons in the dehydrogenation. a) fitted Kissinger curves, b) dehydrogenation activation energy curves.

Fig. 6. Hydrogen desorption content of the $Mg_{67}Ni_{33-x}Y_x$ ribbons.

Fig. 7. The dehydrogenation kinetics curves of the $Mg_{67}Ni_{33-x}Y_x$ (x = 0, 1) ribbons at 523 and 623 K in initial 1 and 0.5 h. a) 523 K in initial 1h, b) 623 K in initial 0.5 h.

Table 1. The dehydrogenation peak temperatures of the hydrogenated $Mg_{67}Ni_{33-x}Y_x$ (x = 0, 1, 3, 6) melt-spun ribbons at heating rates of 5, 10, 15 and 20 K/min.